Cation−Eutectic Transition via Sublattice Melting in $CuInP_2S_6$/$In_{4/3}P_2S_6$ van der Waals Layered Crystals

Michael A. Susner,[*,†,∥,⊥] Marius Chyasnavichyus,[‡] Alexander A. Puretzky,[‡] Qian He,[†] Benjamin S. Conner,[†] Yang Ren,[§] David A. Cullen,[†] Panchapakesan Ganesh,[‡] Dongwon Shin,[†] Hakan Demir,[#] Jacob W. McMurray,[†] Albina Y. Borisevich,[†] Petro Maksymovych,[*,‡] and Michael A. McGuire[*,†]

[†]Materials Science and Technology Division and [‡]Center for Nanophase Materials Sciences, Oak Ridge National Laboratory, 1 Bethel Valley Road, Oak Ridge, Tennessee 37831, United States

[§]X-Ray Science Division, Argonne National Laboratory, Argonne, Illinois 60439, United States

[∥]Aerospace Systems Directorate, Air Force Research Laboratory, 1950 Fifth Street, Bldg 18, Wright-Patterson Air Force Base, Ohio 45433, United States

[⊥]UES Inc., 4401 Dayton-Xenia Road, Beavercreek, Ohio 45432, United States

[#]School of Chemical & Biomolecular Engineering, Georgia Institute of Engineering, 311 Ferst Drive NW, Atlanta, Georgia 30332, United States

* Supporting Information

ABSTRACT: Single crystals of the van der Waals layered ferrielectric material $CuInP_2S_6$ spontaneously phase sepa-rate when synthesized with Cu deficiency. Here we identify a route to form and tune intralayer heterostructures between the corresponding ferrielectric ($CuInP_2S_6$) and paraelectric ($In_{4/3}P_2S_6$) phases through control of chemical phase separation. We conclusively demonstrate that Cu-deficient $Cu_{1−x}In_{1+x/3}P_2S_6$ forms a single phase at high temperature. We also identify the mechanism by which the phase separation proceeds upon cooling. Above 500 K both

Cu^+ and In^{3+} become mobile, while $P_2S_6^{4-}$ anions maintain their structure. We therefore propose that this transition can be understood as eutectic melting on the cation sublattice. Such a model suggests that the transition temperature for the melting process is relatively low because it requires only a partial reorganization of the crystal lattice. As a result, varying the cooling rate through the phase transition controls the lateral extent of chemical domains over several decades in size. At the fastest cooling rate, the dimensional confinement of the ferrielectric $CuInP_2S_6$ phase to nanoscale dimensions suppresses ferrielectric ordering due to the intrinsic ferroelectric size effect. Intralayer heterostructures can be formed, destroyed, and re-formed by thermal cycling, thus enabling the possibility of finely tuned ferroic structures that can potentially be optimized for specific device architectures.

KEYWORDS: 2D ferrielectric, transition metal thiophosphate, sublattice melting, 2D heterostructures, chalcogenides
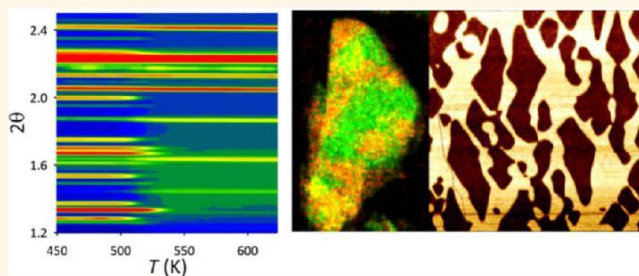
The current era of 2D electronic materials requires new approaches to enable device functionality.[1−6] Tran-sition metal dichalcogenides (TMDs) have been widely studied for their optoelectronic and semiconducting properties, allowing the fabrication of nanocavity lasers,[7] light-emitting diodes,[8,9] and photodetectors.[10] However, thus far the formation of progressively more complicated heterostructures relies either on physical adhesion (as in "stamping" of van der Waals heterostructures, e.g., refs 11 and 12) or on sequential chemical vapor deposition techniques (as demonstrated for BN/C heterostructures, e.g., ref 13). Both of these approaches suffer from limited throughput and extrinsic control over heterostructure formation.

Here, we examine an alternative that relies on thermochem-istry and sublattice melting to produce in-plane heterostruc-tures on a bulk scale using a representative of the materials class called metal thio(seleno) phosphates, or MTPs.[14] These van
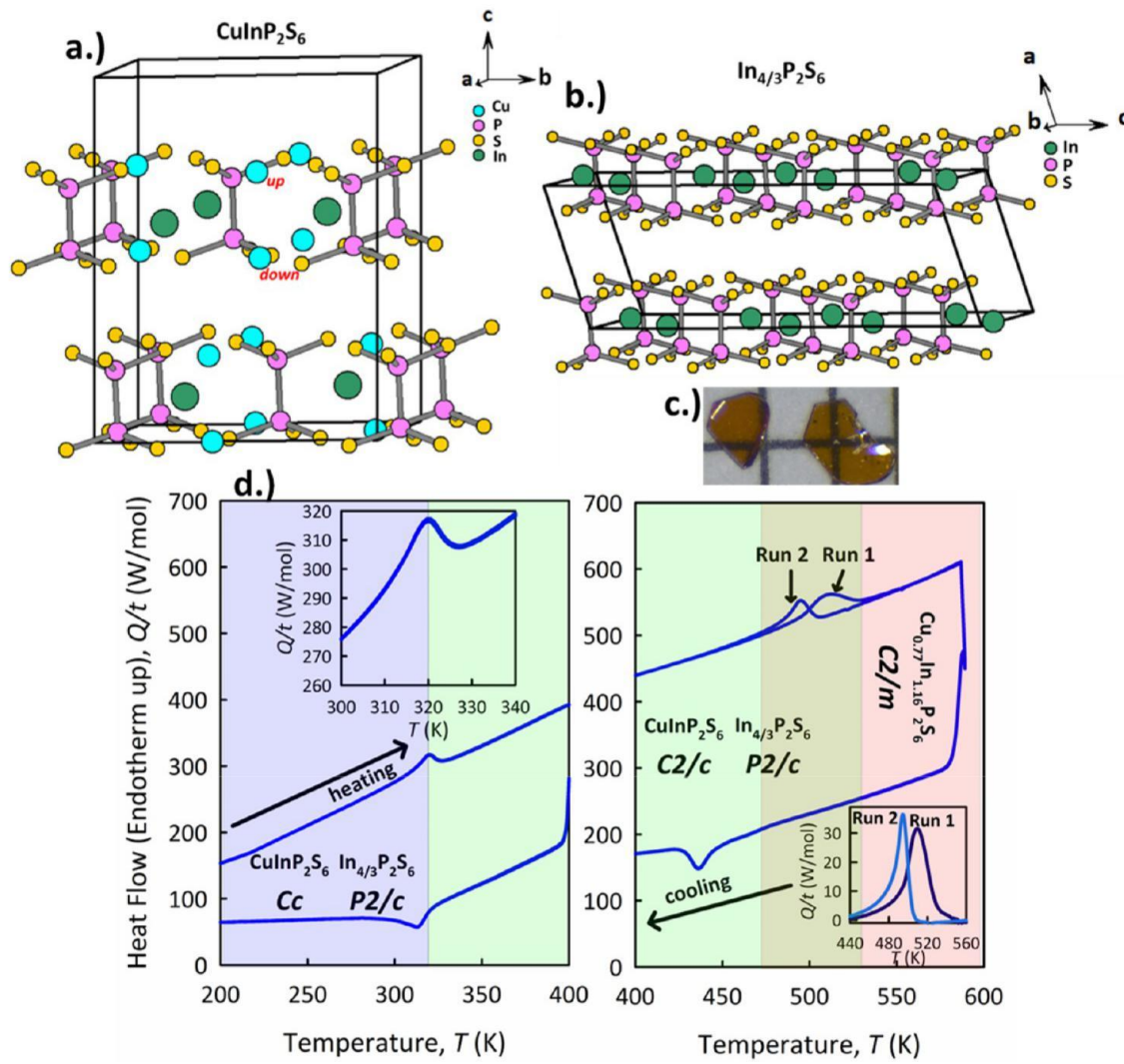
Figure 1. (a) Crystal structure of CuInP$_2$S$_6$ phase denoting the two different Cu locations; (b) crystal structure of In$_{4/3}$P$_2$S$_6$ phase; (c) optical image on a 1 mm × 1 mm grid showing typical sized single crystals containing both phases; (d) DSC plot of CuInP$_2$S$_6$/In$_{4/3}$P$_2$S$_6$ heterostructure (composition Cu$_{0.72}$In$_{1.13}$P$_{2.06}$S$_6$) showing the two phase transitions present as well as the associated structural transitions for each phase. The low-temperature cycling was from 150 to 420 K at a ramp rate of 50 °C/min. Care was taken not to enter into the regime where domain size changed. The order−disorder transition of the CuInP$_2$S$_6$ phase from Cc to $C2/c$ is detailed in the left-hand inset. The high-temperature cycling was performed from 310 to 590 K at 50 °C/min. In the right-hand inset we show the difference between the initial run (where the sample exhibited a coarse phase distribution) and the second run (where the sample exhibited a fine phase distribution). The shading denotes the structures observed via X-ray diffraction: blue, In$_{4/3}$P$_2$S$_6$($P2/c$) and CuInP$_2$S$_6$(Cc); green, In$_{4/3}$P$_2$S$_6$($P2/c$) and CuInP$_2$S$_6$($C2/c$); brown, three-phase region; red, Cu$_{0.77}$In$_{1.16}$P$_2$S$_6$($C2/m$).

der Waals gapped compounds are structured from [P$_2$X$_6$]$^{4-}$ ethane-like building blocks where the close-packed X = S, Se atoms form the van der Waals gap boundaries. Within the material plane are distorted octahedral sites, one-third of which are filled by the P−P dimers, with the remainder of the octahedral sites filled by charge-balancing cations for a final composition of [M^{2+}]$_2$[P$_2$X$_6$]$^{4-}$, M^{1+}M^{3+}[P$_2$X$_6$]$^{4-}$, [M^{3+}]$_{4/3}$[P$_2$X$_6$]$^{4-}$, M^{4+}[P$_2$X$_6$]$^{4-}$, etc. This diversity of cation chemistry within an otherwise nearly identical anion structure allows for the emergence of such correlated behaviors as magnetism,[15−22] ferroelectricity,[23−29] and Mott insulator-type behavior[30] and makes the MTP compounds a possible 2D analogue for complex oxides.[14] It is noteworthy, however, that although the anion lattices of these materials are nearly the same, the cation lattices may or may not be ionically or even structurally compatible. Therefore, this family of materials presents an interesting opportunity among the van der Waals

crystals for bulk nano- and meso-structuring through solid-state chemical processes such as alloying or, conversely, chemical phase separation.

In our earlier work,[26] we demonstrated that the ferrielectric Curie temperature of one specific material, CuInP$_2$S$_6$, can be increased in chemically phase-separated crystals when coexist-ing with paraelectric In$_{4/3}$P$_2$S$_6$.[23,24] To achieve the desired effect, the chemical phase separation needs (1) to avoid defect formation and (2) to occur over a sufficiently large length scales that exceed the ferrielectric correlation volume of CuInP$_2$S$_6$ (which we estimate to be ∼50 nm, based on our studies of the size effect[31]). Both of these requirements are apparently satisfied in CuInP$_2$S$_6$/In$_{4/3}$P$_2$S$_6$, not in the least because of the relatively low phase separation temperature of only ∼500 K, significantly below the decomposition temperature of either compound.

In this work we identify the mechanism by which such phase separation occurs in the $CuInP_2S_6/In_{4/3}P_2S_6$ system (Figure 1), which involves the phenomenon of sublattice melting. Furthermore, we demonstrate that by controlling the cooling rate across the separation temperature we can create metastable crystals with a high degree of control over the average length scale of the chemical phases. In the limit of the strongest chemical confinement, the ferroelectric transition becomes suppressed well below room temperature due to ferroelectric size effects. Simple reheating of the crystal restores the ferroelectric properties back to their original state.

Sublattice melting has been well established for 3D bulk solids of superionic conductors, such as silver and copper halides (e.g., refs 32 and 33), as well as more recently Li-ion conducting electrolytes and electrodes such as LiFePO₄,[34] Li₃PS₄,[35] Li$_x$Nb₂O₅,[36] and Li$_x$VO₂.[37] The essential structural requirements for this type of transition can also be satisfied in certain thiophosphates. In bulk solids, these involve several nearly equivalent crystallographic positions for the ions and comparatively low formation energy of Frenkel defects. In the specific case of $In_{4/3}P_2S_6$, there is a natural 1/3 ratio of vacancy sites in the otherwise complete honeycomb cation lattice, which may obviate the need to create Frenkel defects.

We used detailed calorimetric analyses to determine the temperature of phase separation within single crystals as a function of net Cu/In ratio, and we further employed electron microscopy, micro-Raman spectroscopy, and X-ray diffraction to observe this transition in situ. Based on supportive ab initio defect formation and migration calculations, our overall conclusion is that the thermodynamics of this system can be described as a eutectic transition on the cation sublattice wherein the Cu/In and In/vacancy cation sublattices (representing $CuInP_2S_6$ and $In_{4/3}P_2S_6$, respectively) form two distinct phases within the same single crystal below ~500 K and melt into a single-phase disordered cation solution above this temperature. At the same time, the $[P_2S_6]^{4-}$ framework is preserved across the transition. Our results indicate that the cation sublattice can be described by a phase diagram similar to a binary eutectic. Given the similarity of the $[P_2S_6]^{4-}$ backbone across the transition metal thiophosphate family, our findings will very likely translate to other compositions, dramatically expanding the accessible chemical phase space of this already very diverse class (with over 300 known compositions[14]) and giving control over lateral confinement over ferrielectric, antiferromagnetic, and Mott-insulating phases, as well as photoactive properties without the need to change chemical composition.

RESULTS AND DISCUSSION

In Table 1 we list the compositions we obtained via vapor transport growth procedures together with the ferrielectric transition temperatures (T_C) and the phase separation temperatures (T_S). Typical crystals appeared as shown in Figure 1. The compositions were determined via SEM-EDS and, when plotted against the layer spacing determined by X-ray diffraction, show what at casual inspection appears to be a fully miscible pseudobinary system.[23] However, higher resolution SEM, TEM, and PFM imaging shows there are instead two distinct phases present: $In_{4/3}P_2S_6$ and $CuInP_2S_6$. The transitions listed in Table 1 were determined via thermodynamic measurements and will be discussed in more detail below. As detailed in our previous work,[23] the T_C of the mixed-phase crystals increases as the concentration of Cu is

Table 1. List of Nominal Compositions of $Cu_{1-x}In_{1+x/3}P_2S_6$ Samples Together with T_C and T_S[a]

nominal composition	EDS composition	T_C (K)[b]	T_S (K)[c]
$In_{4/3}P_2S_6$	$In_{1.37(5)}P_{2.02(4)}S_6$		
$Cu_{0.1}In_{1.3}P_2S_6$	$Cu_{0.05(2)}In_{1.36(2)}P_{2.05(1)}S_6$	334.7	506.3
$Cu_{0.2}In_{1.267}P_2S_6$	$Cu_{0.19(4)}In_{1.30(2)}P_{2.03(3)}S_6$	334.0	504.7
$Cu_{0.4}In_{1.2}P_2S_6$	$Cu_{0.42(6)}In_{1.23(5)}P_{2.06(5)}S_6$	328.2	494.4
$Cu_{0.4}In_{1.2}P_2S_6$	$Cu_{0.72(5)}In_{1.13(5)}P_{2.06(5)}S_6$	324.1	495.0
$Cu_{0.4}In_{1.2}P_2S_6$	$Cu_{0.77(3)}In_{1.16(1)}P_{2.03(2)}S_6$	319.7	494.1
$Cu_{0.8}In_{1.067}P_2S_6$	$Cu_{0.99(4)}In_{1.05(3)}P_{2.04(2)}S_6$	307.6	
$CuInP_2S_6$	$Cu_{1.18(7)}In_{1.01(1)}P_{2.01(4)}S_6$	307.7	

[a]The numbers in parentheses denote standard deviations determined from nine or more spectra/points. [b]Measured on heating after cooing at a rate of 0.333 °C/min. [c]Measured on heating after cooling at a rate of 50 °C/min.

reduced. This is to say that the concentration of ferrielectric $CuInP_2S_6$ is reduced but the T_C of the phase is significantly enhanced.

Thermodynamic Characterization. We performed thermodynamic characterization on the samples listed in Table 1 and describe these procedures in detail in the Materials and Methods section. We completed two complementary sets of experiments. In the first set, we ramped temperatures from 150 K to 420 K at 50 °C/min. We show an example of these measurements in the left-hand panel of Figure 1d for a sample with the composition $Cu_{0.72}In_{1.13}P_{2.06}S_6$. We repeated thermal cycling several times, and no difference was observed in the ferrielectric transition temperature, suggesting that the heterostructure is more or less fixed in terms of chemistry for this temperature regime. Details of this lower temperature transition and the phase stability of the $CuInP_2S_6/In_{4/3}P_2S_6$ heterostructure at these temperatures can be found in refs 23 and 31.

In the second set of thermal analysis experiments we took as-grown crystals and performed differential scanning calorimetry (DSC) measurements from 310 to 590 K. Unlike the ferrielectric transition, which was visible for all compositions containing the $CuInP_2S_6$ phase, this transition was noted to exist for only mixed compositions and did not occur in either pure-phase endmember. Moreover, the energy associated with this high-temperature transition follows the enthalpy of mixing maximum defined by $_{mix}H = \Omega x_1 x_2$ where x_1 and x_2 are the fractional components of the two phases, $CuInP_2S_6$ and $In_{4/3}P_2S_6$, and Ω is a constant that determines the nature of the departure from ideal behavior (see Supplemental Figure S1).

An example of such a transition for a sample with the composition $Cu_{0.72}In_{1.13}P_{2.06}S_6$ is displayed in the right-hand panel of Figure 1d. In the high-temperature data, we note a history dependence with respect to the location and distribution of the endotherm, as detailed in the inset of the figure. This suggests that heating to this high temperature results in a structural phase transition. The virgin samples were cooled from their reaction temperature to room temperature at the relatively slow rate of 20 °C/h. The broad endotherm associated with the transformation of the coarse two-phase virgin material to the higher temperature phase (centered at 509 K with a fwhm of 23K) both shifts to a lower temperature (494 K) and narrows (fwhm of 14 K) upon the application of a new thermal history where the sample is fast-cooled back to room temperature at a rate of 50 °C/min, thus forming a

nanometer-sized domain heterostructure (see below). We believe this change is a direct result of the shorter diffusion lengths associated with the fast-cooled material. In Supplemental Figures S2 and S3 we examine the relationships between domain size and latent heat of the high-temperature transition.

Although our original hypothesis was that of spinodal decomposition, the present data rule out this previous assumption (at least at these temperatures)[23] in favor of a first-order structural transition. In order to quantitatively explain the physics behind this high-temperature transition, we performed high-resolution synchrotron X-ray diffraction experiments.

In Situ Observations of the Cation Disorder Transition. We collected diffraction patterns using high-energy synchrotron radiation (λ = 0.117 418 Å) at the Advanced Photon Source at Argonne National Laboratory. We collected data as a function of temperature upon heating for the two endmember compounds ($In_{4/3}P_2S_6$ and $CuInP_2S_6$) and two samples of composition $Cu_{0.42}In_{1.23}P_2S_6$, one as-grown by cooling at 0.333 °C/min from 760 °C and one that had been heated to above the phase separation temperature and then quenched. The latter two samples represent $CuInP_2S_6$/ $In_{4/3}P_2S_6$ heterostructures of the same composition but with different sized domains. We took these data on powder obtained through grinding large single crystals of the materials.

In Figure 2 we present contour plots of XRD patterns collected for the pure-phase $CuInP_2S_6$ and $In_{4/3}P_2S_6$ materials as well as the mixed phase $Cu_{0.42}In_{1.23}P_2S_6$ sample. The $CuInP_2S_6$ pure-phase sample shows a subtle structural transition at ~260−325 K, as is readily evidenced by the change of intensity and/or position of several peaks, most notably for the reflection at 2θ = 3.17° and the two near 4.13°. These anomalies are associated with Cu ordering, a change in space group from Cc to C2/c, and the onset of ferrielectric ordering as previously described.[29] The contour plot of the $Cu_{0.42}In_{1.23}P_2S_6$ mixed-phase sample, in contrast, represents a picture more complicated than a simple mixture of the pure-phase data. The most relevant transition in the context of this paper is observed at a higher temperature, ~520 K. Above this temperature fewer peaks are present, signifying the transition to a single, simpler crystal structure.

Figure 3 and Figure 4 show the temperature dependence of crystallographic parameters of the pure-phase $CuInP_2S_6$ and $In_{4/3}P_2S_6$ materials and the corresponding phases in the mixed-phase $Cu_{0.42}In_{1.23}P_2S_6$ sample (for details, see Table S1). We determined these values from the Rietveld refinement of the synchrotron XRD data over the range 113−603 K. The $CuInP_2S_6$ data (Figure 3a) clearly show the structural transition related to the Cu ordering near 300 K. The lattice parameters a, b, and c all increase upon heating through the ferrielectric transition, but change is most prominent for the stacking direction, in this case c, consistent with previous reports (e.g., ref 29). Lattice parameters of $In_{4/3}P_2S_6$ (Figure 3b) vary smoothly with temperature over this same temperature range, showing no indication of any phase transitions. A much higher temperature transition from P2/c to $R\bar{3}$ at 945 K has been reported in $In_{4/3}P_2S_6$ due to disordering of the In and vacant sites within the still-ordered P_2S_6 framework.[35]

We obtained the analysis of the mixed-phase $Cu_{0.42}In_{1.23}P_2S_6$ in Figure 4 using a Rietveld procedure with the established low-temperature structure ($P2_1/c$) for $In_{4/3}P_2S_6$ and using a LeBail method for the lattice parameters of the $CuInP_2S_6$ phase. Like
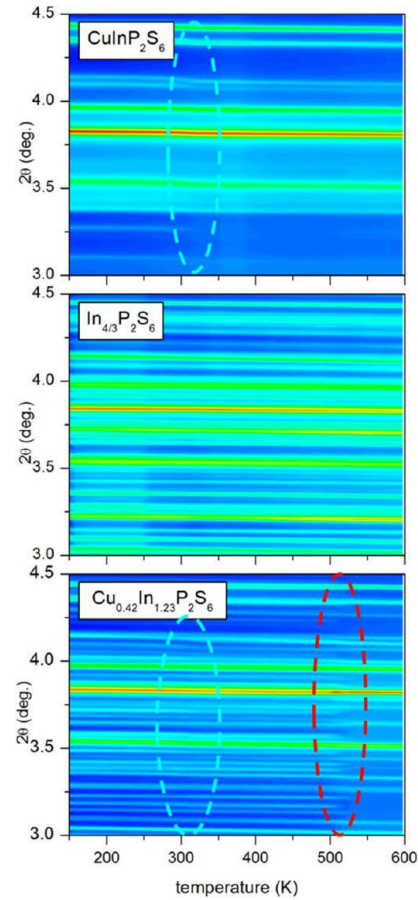

Figure 2. Contour plots of synchrotron X-ray diffraction (XRD) patterns (λ = 0.117418 Å) over the range of 150−600 K for pure-phase $CuInP_2S_6$ and $In_{4/3}P_2S_6$ as well as mixed-phase $Cu_{0.42}In_{1.23}P_2S_6$. The low-temperature transitions are circumscribed by a blue-colored dashed line, while the high-temperature transition is outlined in red.

the pure-phase $CuInP_2S_6$, the $CuInP_2S_6$ phase embedded in the $Cu_{0.42}In_{1.23}P_2S_6$ heterostructure exhibits a clear phase transition that is most apparent in the c-axis (Figure 4c). The a and b lattice parameters also show structural anomalies in the 240− 332 K range (Figure 4a and b), although not as prominent as the pure-phase material. Interestingly, the thermal lattice response in the $In_{4/3}P_2S_6$ component is also observed at the T_C of the $CuInP_2S_6$ component, which likely reflects interfacial effects between the two chemical phases.

From comparison of the layer spacings in pure endmember phases with those observed for $Cu_{0.42}In_{1.23}P_2S_6$ (Figure 5), we conclude that the heterostructure formation compresses $CuInP_2S_6$ and expands $In_{4/3}P_2S_6$ along the stacking direction. Similarly for the in-plane behavior, $CuInP_2S_6$ is compressed while $In_{4/3}P_2S_6$ is expanded in the heterostructure, as judged from the in-plane area per P_2S_6 unit in one layer of each phase (Figure 5). In our previous work we noted that the chemical pressure induced by the presence of the added $In_{4/3}P_2S_6$ resulted in the T_C enhancement in the heterostructured material,[23] in accord with experiments that noted a similar effect where external mechanical pressure was applied.[39] From our present diffraction data we see that this chemical pressure is caused by compression in both the stacking direction and within the layer. This compression presumably increases the depth of the potential well for Cu to sit in the "up" position in
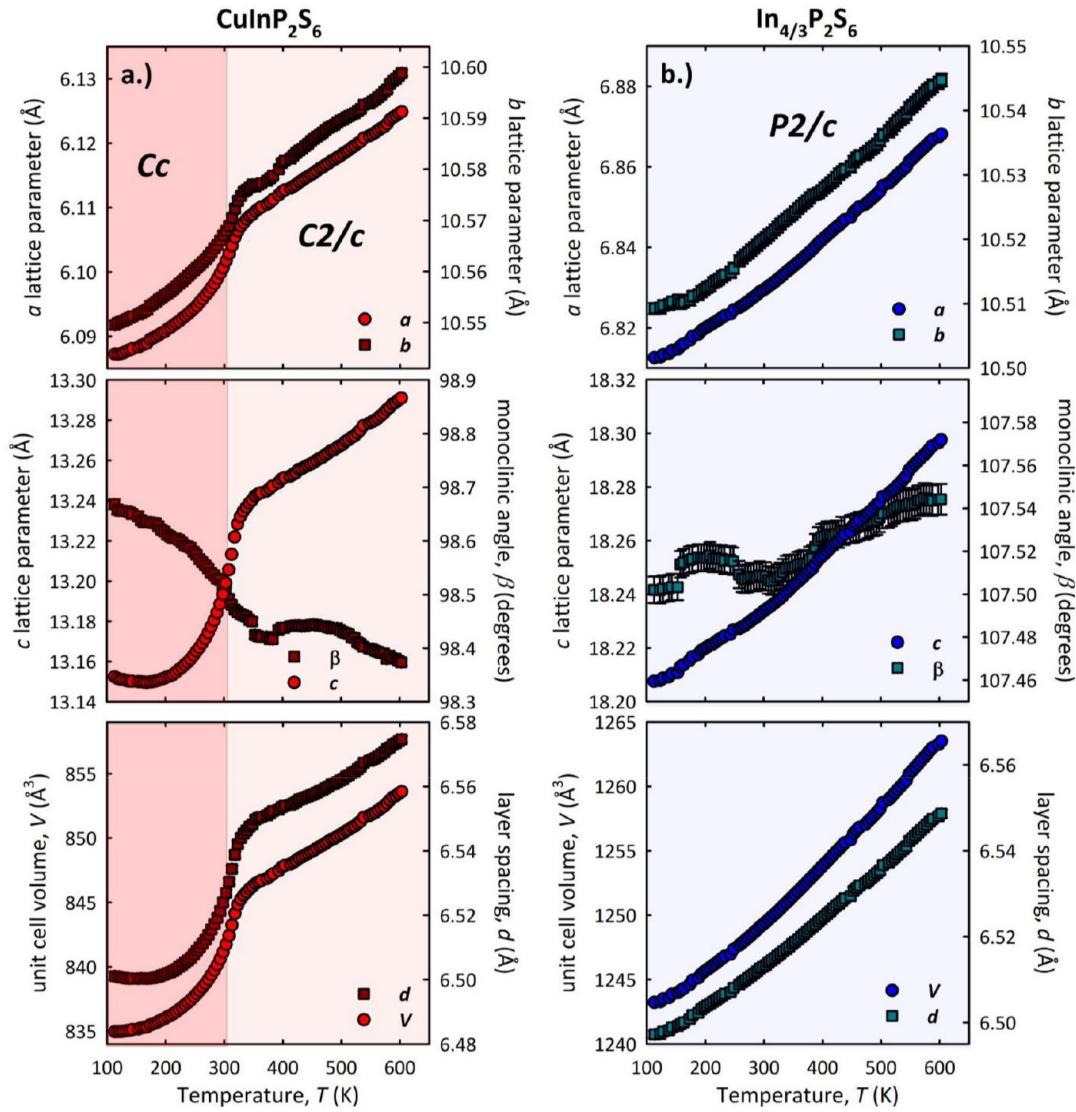
Figure 3. Crystallographic parameters elucidated from Rietveld refinement of the synchrotron XRD data for (a) $CuInP_2S_6$ and (b) $In_{4/3}P_2S_6$. The layer spacing d is defined as the distance between the midplane of two adjacent layers, equivalently the sum of the thickness of one lamella and one van der Waals gap. The shaded regions in (a) delineate the low-temperature ferrielectric phase (Cc) from the high-temperature paraelectric phase ($C2/c$).

the octahedral cage (Figure 1); however, the exact energetics of this system have yet to be quantified. We present the same structural analyses for the quenched heterostructured sample in Supplemental Figures S4 and S5.

The transition to the high temperature (HT) phase in $Cu_{0.42}In_{1.23}P_2S_6$ appears near 500 K (Figure 6) and is complete by 563 K, as judged by X-ray diffraction (XRD). There exists a broad region of diffuse scattering from 2θ values of ~1.2−2.0° (Figure 6a), which is not present in any of the pure-phase compounds and is likely related to chemical disorder (perhaps dynamic) and potential short-range order in the HT phase. In Figure 6b, we present a contour plot of the data through the high-temperature phase transition. Using the peak labels to the right, one may clearly discern the presence of the three-phase region and the emergence of the single high-temperature phase. The full refinements of the three-phase data sets were not stable, so only the data for the HT phase is shown for temperatures above 573 K.

We tried several established MTP structures (including the $CuInP_2S_6$ and $In_{4/3}P_2S_6$ structures) to model the HT phase and

found that a modification of the $Fe_2P_2S_6$ structure[40] (the prototype structure of the MTP materials class[41]) with space group C2/m yielded the best fit (Figure 6c). Each Fe site in $Fe_2P_2S_6$ was replaced with a mixture of In at the cage centers, Cu distributed equally over up and down positions (Figure 1a), and vacancies. This model is shown in Figure 6d. Detailed structural information can be found in Supplemental Table S2. This structure served to account for nearly every peak present in the high-temperature diffraction pattern and matches intensities quite well over the entire angular range. The best fit is achieved with 30.4% Cu, 62.8% In, and 6.8% vacancy per octahedral cage. Considering the complexity of the model, these are in reasonable agreement with the values expected based on the chemical composition of the sample: 21% Cu, 59% In, and 20% vacancy. As noted above, the diffuse maximum present between 1.2° < 2θ < 2.0° may be related to the cation/vacant site disorder. These angles correspond with d spacings of 3.4−6.7 Å, matching the nearest-neighbor and next-nearest-neighbor spacings of the metal sites.
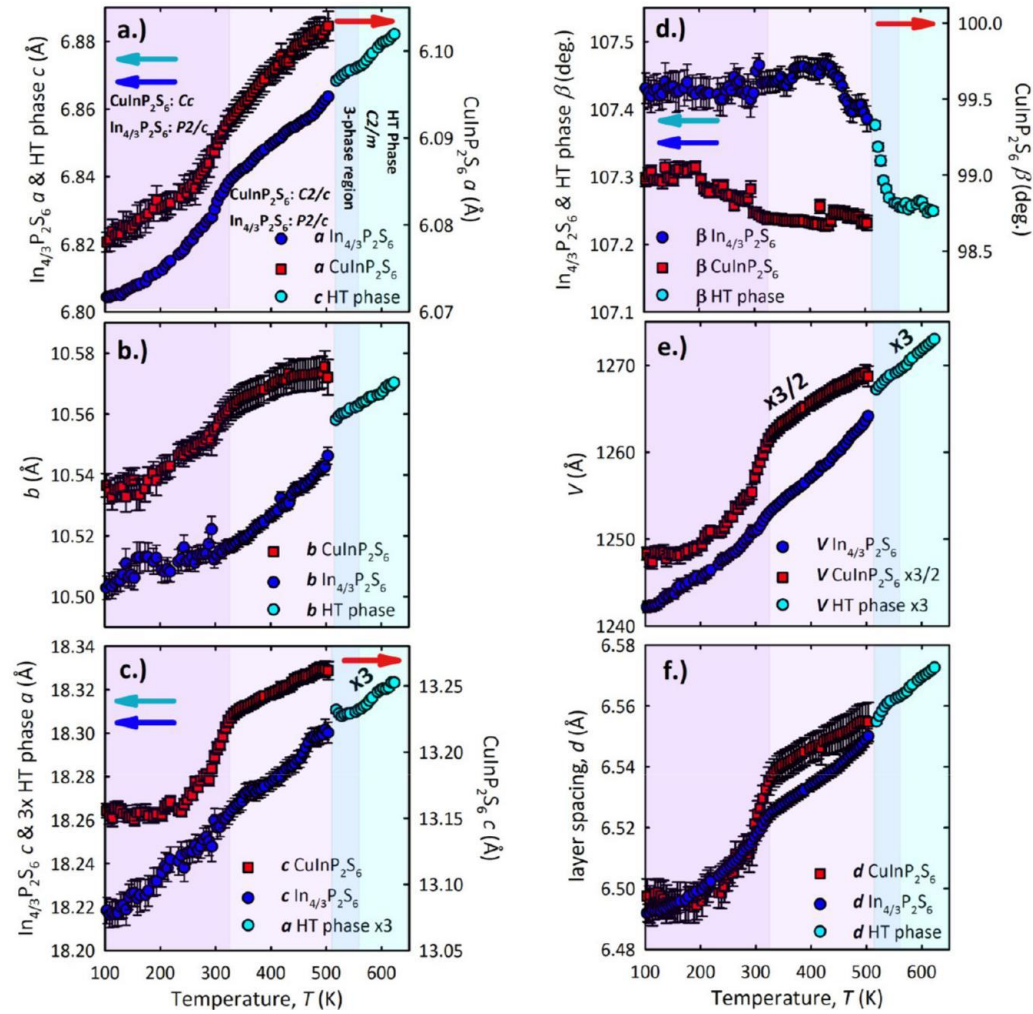
Figure 4. Material parameters elucidated from refinement of the synchrotron XRD data for $Cu_{0.42}In_{1.23}P_2S_6$. The colored arrows point to the appropriate axis for the like-colored plots. (a) a lattice parameters for $CuInP_2S_6$ and $In_{4/3}P_2S_6$ and the c lattice parameter for the HT phase; (b) b lattice parameters for all three phases (note that all three phases are plotted to the same scale); (c) c lattice parameters for $CuInP_2S_6$ and $In_{4/3}P_2S_6$ and the a lattice parameter for the HT phase (the a lattice parameter of the HT phase has been multiplied by a factor of 3 to better show its relationship with the c lattice parameter of $In_{4/3}P_2S_6$); (d) monoclinic angle, β, for all three phases; (e) unit cell volume for all three phases (note that all three phases are plotted to the same scale and that the unit cells of the $CuInP_2S_6$ and HT phases have been multiplied by 3/2 and 3, respectively, to better show their geometric relationships); and (f) layer spacing, of all three phases (note that all three phases are plotted to the same scale). From left to right, the different shaded regions represent (1) the two-phase region of $CuInP_2S_6$ (Cc) and $In_{4/3}P_2S_6$ (P2/c); (2) the two-phase region of $CuInP_2S_6$ (C2/c) and $In_{4/3}P_2S_6$ (P2/c); (3) the three-phase region of $CuInP_2S_6$ (C2/c), $In_{4/3}P_2S_6$ (P2/c), and the high-temperature phase of $Cu_{0.42}In_{1.23}P_2S_6$ (C2/m); (4) the single-phase HT phase of $Cu_{0.42}In_{1.23}P_2S_6$ (C2/m).

To further study the chemical disordering transition in $Cu_{0.42}In_{1.23}P_2S_6$, the chemical composition of the heterostructure was mapped using energy dispersive spectroscopy (EDS) conducted in a transmission electron microscope (TEM) at various temperatures. On the left-hand side of Figure 7, we present TEM images of one of the $Cu_{0.42}In_{1.23}P_2S_6$ samples that was previously slow-cooled from the HT phase at 20 °C/h. On the right-hand side of Figure 7a we show EDS maps of Cu and In. Near 295 K we see that the Cu and In concentrations are modulated over the particle area. Maps of P and S showed uniform distributions.

At 480 K, the Cu appears to be more diffuse than at lower temperatures. This process continues at 510 K, correlating well with the emergence of the three-phase region in Figure 4 and Figure 5. At 560 K, we note that the Cu and In EDS maps show that these elements are homogeneously distributed over the entirety of the crystal. This coincides with the single-phase region seen in the synchrotron XRD data in Figure 4 and

further confirms the presence of the homogeneous HT phase of $Cu_{0.42}In_{1.23}P_2S_6$.

Thermal Cycling, Quenching, and Domain Size Effects. We have previously established that we can control the size of the chemical domains in the $CuInP_2S_6/In_{4/3}P_2S_6$ heterostructure by varying the ramp rate from high temperature.[23] Here we examine this in more detail using TEM, X-ray diffraction, and scanning probe techniques. Additional STEM-EDS spectrum images were collected on the specimen after cooling from the single high-temperature phase back to room temperature at different rates in the TEM. Quenching of this sample to room temperature at a rate greater than 100 °C/min results in a microstructure that looks qualitatively similar to that obtained at 560 K (Figure 7, "Quench"). However, very small chemical domains may be discerned in the quenched sample (see Supplemental Figure S6). Slowing the cooling rate to 50 °C/min from an initial temperature of 560 K results in the formation of domains on the order of ~50 nm in size (cf.
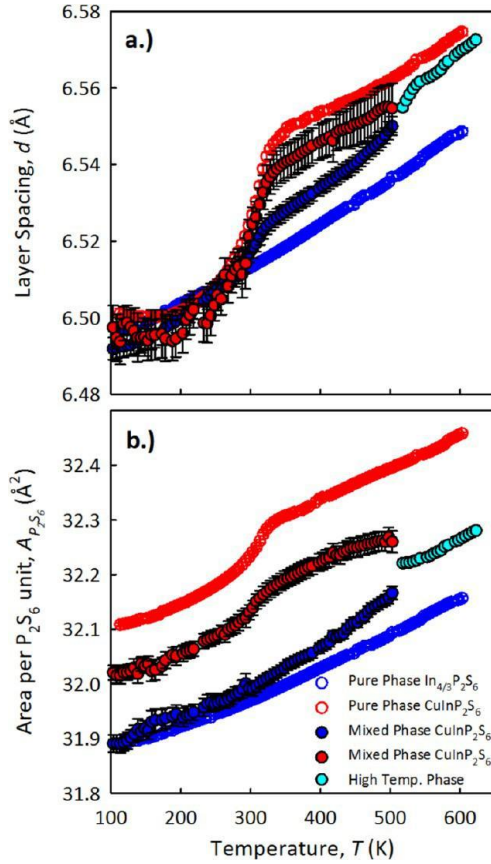
Figure 5. Comparison of the layer spacing and the in-plane area, normalized per P_2S_6 unit, of pure $In_{4/3}P_2S_6$ and $CuInP_2S_6$ (open blue and red symbols, respectively) and $In_{4/3}P_2S_6$ and $CuInP_2S_6$ in a heterostructured alloy of average composition $Cu_{0.42}In_{1.23}P_2S_6$ (solid blue and red symbols, respectively). Data for the high temperature phase are also shown (aqua symbols).

Figure 6a and Supplemental Figure S6). After cooling at a rate of 0.2 K/min, close to that used during initial crystal growth, the domains formed are the same size as the domains as initially imaged in the as-grown sample (cf. Figure 7 top left and bottom right). The spatial distribution of the domains, however, is changed, indicating that the chemical domains are not energetically pinned. Qualitatively, these data support the existence of a single phase above 500 K and a significant degree of reversibility of the chemical phase separation.

The spatial distribution of chemical domains was readily accessible via phase-contrast tapping mode atomic force microscopy. (Figure 8). We applied this technique to analyze the difference between the microstructures of an as-grown crystal (cooled at 20 °C/h from the reaction temperature) compared to that of samples from the same growth cooled at different ramp rates from above the high-temperature transition. The contrast in these images is due to differences in electrostatic or adhesive properties of the contact between the two different chemical phases. These images, presented in Figure 8, show in clear detail the differences in the sizes of the chemical domains, consistent with the EDS observations.

The size of the $In_{4/3}P_2S_6$ domains in the as-cooled sample is on the order of 1−2 μm. Fast cooling the heterostructured sample from above the high-temperature transition yields what appears to be much smaller $In_{4/3}P_2S_6$ and $CuInP_2S_6$ domains (down to ∼10 nm, Figure 8). Moreover, the average size can be

reproducibly controlled via the cooling rate. Faster cooling rates produce a tiered structure with respect to chemical phases; rather than larger single $In_{4/3}P_2S_6$ domains we see a shift to clusters of ever-smaller chemical domains, even at the fastest cooling rates studied. From our previous report on the ferroelectric size effect, ferrielectric order in the pure-phase $CuInP_2S_6$ is progressively suppressed below 50 nm of thickness to the point where it completely vanishes at room temperature by 10 nm.[31] When we translate these results to the $CuInP_2S_6$/ $In_{4/3}P_2S_6$ heterostructures under current investigation, we would expect that ferrielectric behavior would also be largely suppressed as a function of cooling rate (i.e., as the size of the $CuInP_2S_6$ gaps separating the $In_{4/3}P_2S_6$ chemical domains is reduced). We have plotted in Supplemental Figure S7 the evolution of the width of the $CuInP_2S_6$ domains with cooling rate. On the basis of these data, we would expect ferrielectricity to begin to be suppressed at a cooling rate of ∼2 °C/min, concomitant with the appearance of two different length scales of $In_{4/3}P_2S_6$ domain. These chemical domain clusters result in regions where the $CuInP_2S_6$ matrix is reduced in width (and, based on our previous report,[23] thickness) to less than 50 nm.

We used micro-Raman spectroscopy to more quantitatively analyze changes in Cu ordering with respect to domain size evolution (Figure 9a−c) as Raman scattering is very sensitive to small structural distortions.[42] We performed experiments on heterostructured samples with the composition $Cu_{0.42}In_{1.23}P_2S_6$ with one sample representing the as-synthesized (i.e., slow-cooled) material and the other being a material heated above the high-temperature transition and quenched to 0 °C. In Figure 9a we show the evolution of the Raman spectra for both samples as functions of temperature. The slow-cooled sample shows a gradual evolution in the Raman spectra whereby the peaks at ∼100, ∼315, and ∼559 cm^{-1} (indicated by the gray dashed lines) are gradually reduced at temperatures above T_C. These Raman peaks represent anion deformation modes associated with the deformation of the S_6 octahedra surrounding the Cu cations[43] (and to a lesser extent, the In cations, which partially compensate antiparallel to the Cu ordering, cf. Figure 1). The even distribution between the "up" and "down" positions above T_C results in these peaks being suppressed at these elevated temperatures. In Figure 9b we plot the measured intensity of the Raman mode centered at 315 cm^{-1} vs temperature and show that this transition matches well with the aforementioned XRD data with respect to defining the ferrielectric transition. Interestingly, after holding at the maximum temperature (443 K) for several minutes and then rapidly cooling back to room temperature at a rate of 20 °C/ min, the 315 cm^{-1} peak is partially suppressed, suggesting that at temperatures below the high-temperature structural tran-sition chemical domains are likely beginning to coarsen.

In contrast, the quenched sample shows no real evolution with temperature. In Figure 9c we plot the Raman spectrum of the slow-cooled sample at 299 K together with a spectrum of the same sample at 443 K and the room-temperature spectrum of the quenched sample. The spectrum of the slow-cooled sample elevated to higher temperatures very closely resembles the spectrum collected for the quenched sample at 300 K, directly confirming that Cu cation ordering has been greatly suppressed in this sample through nanoconfinement of the $CuInP_2S_6$ chemical domains.

We can further quantify the low-temperature ferrielectric transition from a structural point of view by comparing the ferrielectric transition of the $CuInP_2S_6$ phase for three separate
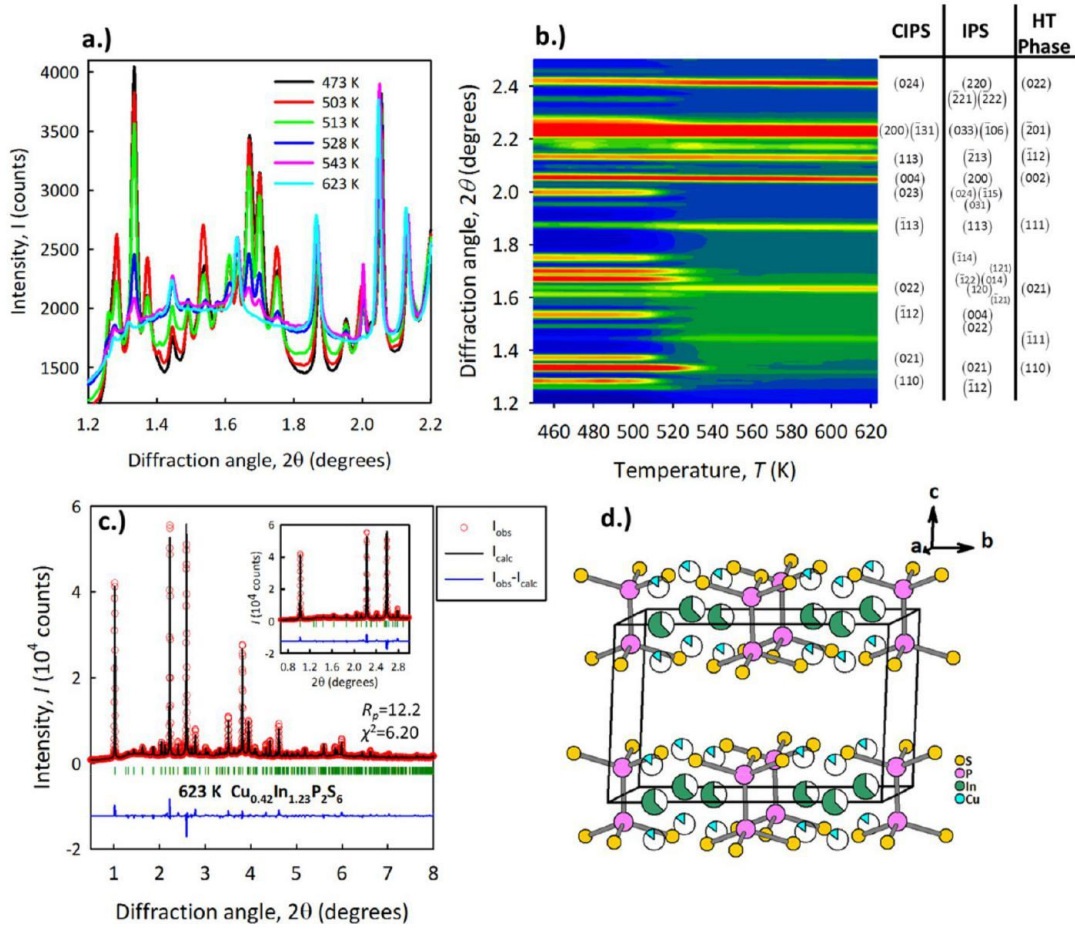
Figure 6. (a) Selection of XRD patterns ($\lambda = 0.117\ 418$ Å) showing the high-temperature evolution of the heterostructured $Cu_{0.42}In_{1.23}P_2S_6$ compound; (b) contour plot of high-temperature phase transformation (the region of diffuse scattering may be spotted as the green region in the lower-right quadrant of the graph); (c) Rietveld refinement of the high-temperature phase of $Cu_{0.42}In_{1.23}P_2S_6$; (d) structure of high-temperature phase showing the refined site occupancies on the metal site (30.4% Cu, 62.8% In, 6.8% vacancy).

materials using our high-resolution synchrotron data: (1) pure $CuInP_2S_6$, (2) $CuInP_2S_6$ embedded in the slow-cooled $CuInP_2S_6/In_{4/3}P_2S_6$ heterostructure, and (3) $CuInP_2S_6$ embedded in the quenched material. Analysis of the XRD data from the quenched sample shows that both the $CuInP_2S_6$ and $In_{4/3}P_2S_6$ phases are present even for the fastest quench rate (i.e., no HT phase was retained). However, significant structural differences from the slow-cooled sample were also present. In Figure 9c we focus on the layer spacing, d, of the $CuInP_2S_6$ phases elucidated from pure-phase, slow-cooled, and quenched material. The layer spacing is the structural parameter most affected by the ferrielectric−paraelectric transition and is therefore useful in telling us if there is any relationship between the domain size and the ultimate size limit of the ferrielectric phase. At the temperature extrema, the layer spacings of the two heterostructured materials (slow-cooled and quenched) are very similar. In the quenched material the structural transition at ~315 K appears largely suppressed, in accord with the Raman data presented above. This ability to control ferroic behavior in a material through nanoconfinement is an exciting opportunity for the engineering of nanostructured devices, especially if this phenomenon can be manipulated via patterning. One can envision the possibility of domain patterning using localized laser heating, where ferrielectrically active regions can be "quenched" into a nonfunctional paraelectric state.

Sublattice Melting. The ionic nature of the MTP family in general and the $CuInP_2S_6/In_{4/3}P_2S_6$ system in particular allows the structure to be considered as a rigid $[P_2S_6]^{4-}$ anion sublattice containing metal cations within the distorted octahedra necessary for stability and charge balance (Figure 1). This P_2S_6 sublattice is constant among the MTP family. In the specific context of this work, it is also constant across the high-temperature transition $CuInP_2S_6$ (C2/c) + $In_{4/3}P_2S_6$ (P2/c) → $Cu_{1-x}In_{1+x/3}P_2S_6$ (C2/m). We can thus ignore this sublattice and instead focus our attention exclusively on the cation sublattice. Similar approaches have been previously used to describe phase transitions in CaF_2,[44] PbF_2,[45,46] AgI,[32,46] $AgBr$,[46] and $AgCl$,[46] among other structures. This framework allows us to simplify the picture to that of a simple sublattice eutectic system.

Combining our experimental DSC data with the data of Gebesh et al.[38] for the $In_{4/3}P_2S_6$ compound allows us to create a phase diagram for the $CuInP_2S_6/In_{4/3}P_2S_6$ system (Figure 10a). In this diagram, we plot the ferrielectric transition and the cation sublattice eutectic liquidus based on the peak maxima of the heating endotherm derived from the DSC data.

We found it difficult to synthesize compositions for the Cu-rich side of the phase diagram, thus suggesting a more complicated thermodynamic picture for these particular chemistries. The In-rich side of the phase diagram is also interesting in that $In_{4/3}P_2S_6$ undergoes an order−disorder

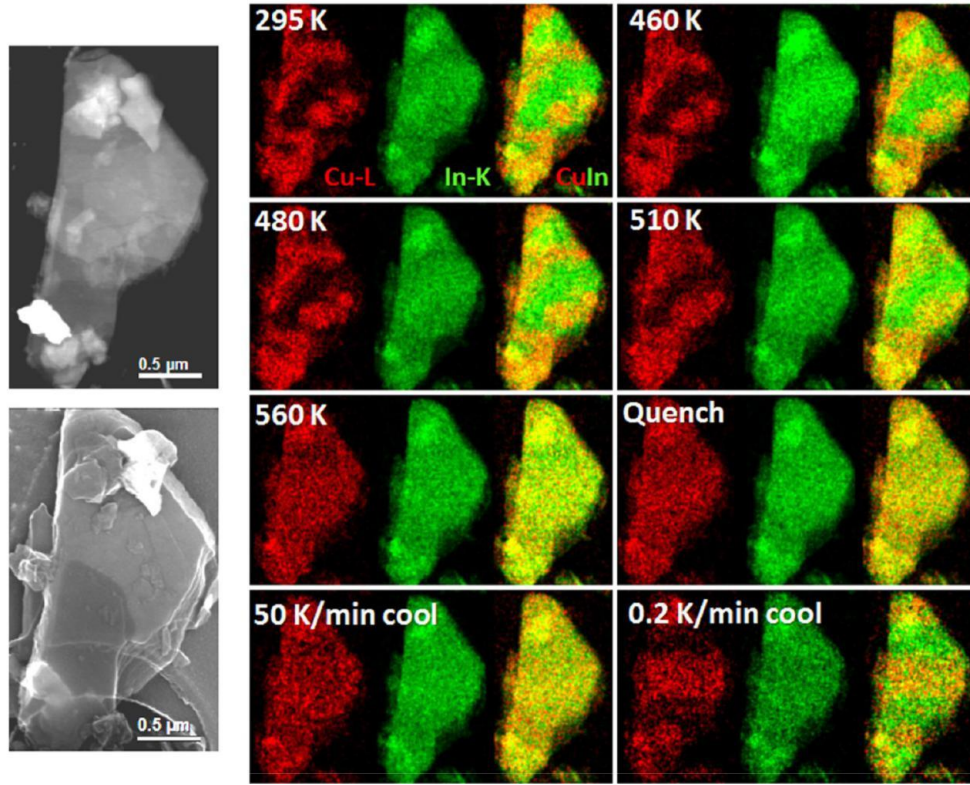Figure 7. In situ STEM-EDS spectrum imaging of the $CuInP_2S_6/In_{4/3}P_2S_6$ heterostructure ($Cu_{0.42}In_{1.23}P_2S_6$) at various temperatures. The two images to the left of the EDS maps are dark field (top) and secondary electron (bottom) images of the crystal. The bright spots in the images to the left represent other phases whose chemistry does not change upon heating. Prior to imaging, the sample was heated to 573 K and cooled to room temperature at 0.2 °C/min. The spectrum images denoted 295, 460, 480, 510, and 560 K represent images taken upon heating of this sample. The three remaining spectrum images represent the sample chemical domain distribution upon heating to above the high-temperature phase transition and subsequent cooling at the noted rate.
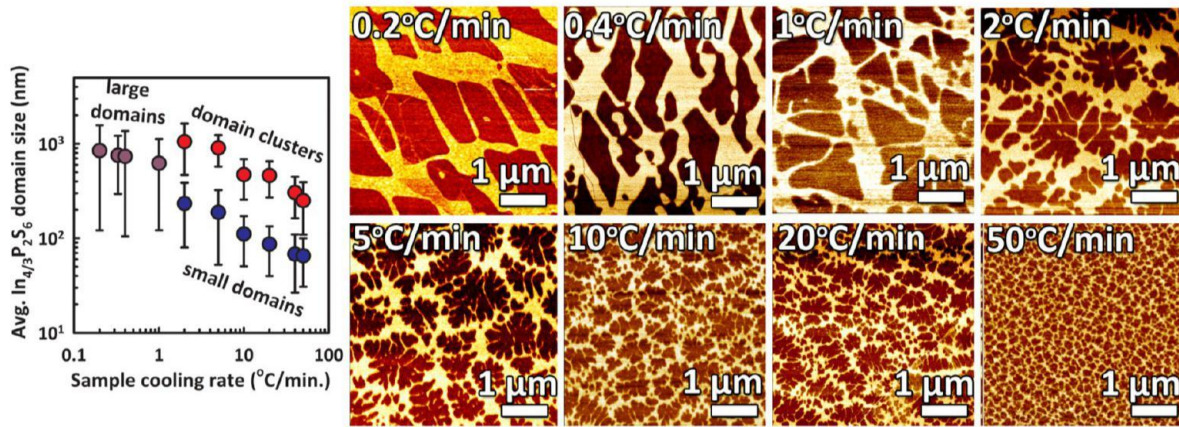

Figure 8. Investigation of $CuInP_2S_6/In_{4/3}P_2S_6$ heterostructured samples cooled at different ramp rates from above the cation liquid temperature. The dark phase represents $In_{4/3}P_2S_6$, while the lighter phase represents $CuInP_2S_6$. The graph shows the relationship between cooling rate and domain/cluster size.

transition in its cation/vacant site sublattice below the thermal decomposition temperature but yet well above the high-temperature phase transition we describe.[38] Clearly, the combination of In, off-center Cu, and vacant sites creates a synergistic effect in which the temperature of cation lattice melting can be lowered to the relatively accessible temperature of ~500 K. The exact interplay between cation ratio, vacant site concentration, and cation diffusion will be the subject of a future investigation. However, preliminary density functional theory (DFT)-based ab initio calculations suggest that the in-plane hopping barrier for a Cu(In) vacancy is ~0.23 eV (~0.75 eV), while the formation enthalpy difference for Cu(In) vacancies is 9 meV (~242 meV) between the hopping sites; these results suggest that it is feasible for the cations to form a sublattice melt where the kinetic energy is above the activation energy for ionic motion.

In Figure 10b, we plot a schematic of what we believe is the eutectic phase diagram of the In−Cu-vacancy cation sublattice. The dashed lines are guides to the eye. The solidus we propose matches well with the appearance of the three-phase region in
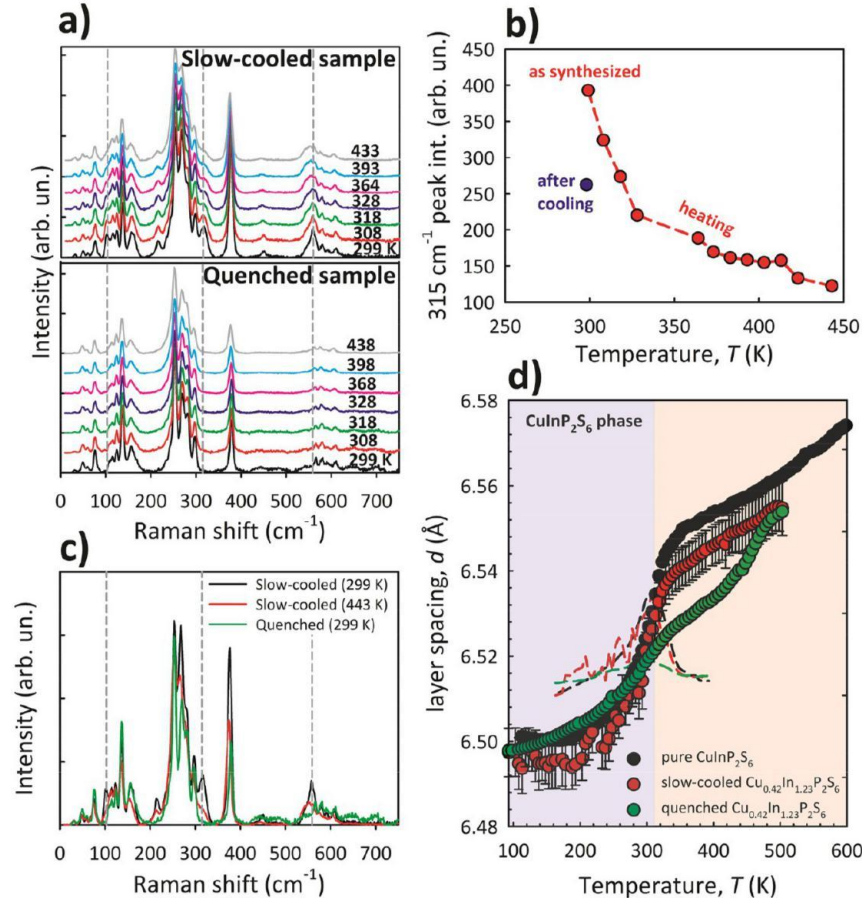
Figure 9. (a) Raman spectra collected at different temperatures with subtracted photoluminescence background. In the quenched sample no major changes are noted, signifying that the ferrielectric transition has been suppressed, in contrast to the slow-cooled sample, where some Raman peaks associated with structural distortions in the S_6 octahedra that are coupled to the Cu cation ordering are suppressed as temperature increases (gray dashed lines indicated at ~100, ~315, and ~559 cm^{-1}). (b) Height of Raman mode at 315 cm^{-1} in slow-cooled sample vs temperature. (c) Comparison of Raman spectra of slow-cooled sample (299 and 443 K) to that of the quenched sample (299 K). (d) Comparison of the layer spacing determined from diffraction data for pure CuInP2S6, slow-cooled heterostructured Cu0.42In1.23P2S6, and quenched Cu0.42In1.23P2S6. The derivative plots for the transition are represented by the dashed lines.
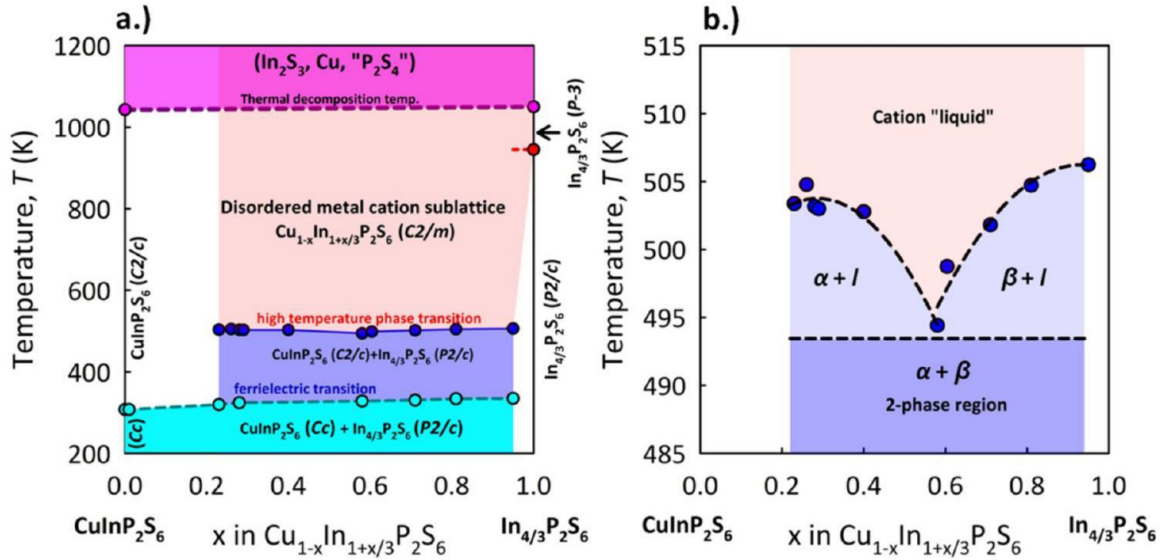
Figure 10. (a) Proposed phase diagram of the CuInP2S6/In4/3P2S6 system based on thermodynamic characterization and high-resolution synchrotron data paired with the existing thermodynamic data of Gebesh et al.;[38] (b) expanded view of the binary eutectic region of the phase diagram (with respect to the cation sublattice).

the XRD data (cf. Figure 4). Compared to the diffraction data presented above, the liquidus extracted from the DSC data is ~20−30 K lower, likely because the DSC data are taken using fast-quenched samples (cf. Figure 1d) where surface energies in nanoscaled materials can serve to depress the phase transition temperature according to the well-known Gibbs−Thomson effect.[47] The uppermost line in Figure 10a represents the thermal decomposition temperature of the material, which is nearly equal for both endmembers (~1060 K)[23,38] but is made difficult to measure due to the high vapor pressures of P and S, which require high pressures for more detailed analysis.

CONCLUSIONS

We had previously reported that $Cu_{1-x}In_{1+x/3}P_2S_6$ showed promising ferrielectric properties in that the T_C could be increased by ~40 K via altering the chemistry and therefore the interfacial strain in this spontaneously heterostructured materi-al.[23] This system is remarkable in that two phases exist simultaneously within the same single crystal and that this phase separation is kinetically tunable with respect to length scale of the phase separation. Here, we have used high-temperature X-ray diffraction and electron microscopy together with differential scanning calorimetry and micro-Raman spectroscopy to conclusively and quantitatively describe the high-temperature phase from which both the ferrielectric and paraelectric domains (i.e., the $CuInP_2S_6$ and $In_{4/3}P_2S_6$ phases) originate within a crystal of this material. At high temperatures a single phase does indeed exist with a structure similar to that of the prototype compound for the metal thiophosphate materials class, $Fe_2P_2S_6$,[40] with the cation sites occupied by a disordered mixture of In, off-center Cu, and vacancies. It is very likely that at these same temperatures the system undergoes transition to a superionic state, which will be investigated in the future. We propose that a simple cation sublattice melting model describes our observations well. This model is based on a simple binary eutectic system and can be described by the equation L → α + β upon cooling through the eutectic point. We stress that this high temperature transition is interesting for two reasons: (1) it occurs within a coherent crystalline framework (i.e., the P_2S_6 anion sublattice), and (2) upon freezing, the disordered cation sublattice phase separates into two distinct phases, one of which is functional ($CuInP_2S_6$). Moreover, the functionality of this $CuInP_2S_6$ ferrielectric phase is determined by the details of that phase separation (i.e., nanoconfinement of the ferrielectric $CuInP_2S_6$ domains suppresses ferroic ordering), opening up opportunities for precision control of lateral heterostructures in layered (and potentially 2D) materials.

MATERIALS AND METHODS

Synthesis of $Cu_{1-x}In_{1+x/3}P_2S_6$ Single Crystals. We synthesized $Cu_{1-x}In_{1+x/3}P_2S_6$ single crystals (Figure 1) through the vapor transport method, following procedures previously described,[23] to make the compositions listed in Table 1. Starting materials, sealed in fused silica ampules, were heated to 750−775 °C at a rate of 30 °C/h and held at that temperature for 4 days and then cooled at a rate of 20 °C/h. We determined the final bulk compositions using a Hitachi TM-3000 scanning electron microscope equipped with a Bruker Quantax 70 energy dispersive X-ray spectrometer using K-lines for Cu, P, and S and L-lines for In. We sampled each composition at least three times on three different samples. The sampling areas were on the order of ~1000 µm, much greater than the chemical domain size, and therefore represent an average of the bulk composition. The EDS analysis on the

$CuInP_2S_6$ and $In_{4/3}P_2S_6$ endmembers resulted in compositions close to the stoichiometric values.

Thermodynamic Characterization. We performed thermal analysis using a PerkinElmer differential scanning calorimeter. We collected data using three different complementary techniques. In the first, we placed "virgin" samples (i.e., samples grown via furnace conditions) in the DSC; we both heated the samples to 420 K and subsequently cooled them at 50 °C/min so as to maximize peak intensity in this energetically subtle transition. We used He purge gas for these low-temperature measurements. These experiments resulted in overlapping data, signifying that no chemical change was present and that the structural transition associated with the ferrilelectric state below 309 K was fully reversible. The second set of experiments involved a similar procedure except that we ramped the temperature from 310 to 590 K using Ar as the purge gas. In these experiments, we noted a sample history dependence resulting from domain reorganization. The third set of experiments involved placing virgin samples in the DSC and heating to high temperatures (590 K) at a rate of 20 °C/min. We then immediately cooled the samples at ramp rates of 50, 40, 20, 10, 5, 2, 1, 0.4, 0.2, and 0.1 °C/min. This sample set therefore consisted of material with varied domain sizes. These samples were then heated back through the chemical phase transition at the same rate of 20 °C/min for direct intercomparison.[48] These last results are presented in the Supporting Information. Temperature and enthalpy calibrations were performed with both In and Sn (A.A. Puratronic 99.999% purity).

Atomic Force Microscopy. For atomic force microscopy imaging, we prepared thin (several hundreds of micrometers) flakes by peeling crystals using the Scotch tape method and depositing them onto the surface of carbon tape mounted onto metal pucks. We performed imaging in tapping mode using a commercial system (Bruker Dimension Icon) while recording both topographic and phase contrast information. The phase-contrast revealed distinct chemical domains due to the difference in adhesive and electrostatic forces in the contact. All sample preparation and measurements were performed inside an Ar-filled glovebox (MBraun). We used ImageJ to analyze the phase-contrast images. $In_{4/3}P_2S_6$ domain size length was determined through taking the root of an area trace.

Raman Measurements. We collected Raman spectra using a custom-built high optical throughput micro-Raman system with a continuous-wave 532 nm solid-state laser (Excelsior, Spectra-Physics) as an excitation source and a 50× long working distance microscope objective with a numeric aperture of 0.5. A typical excitation laser power was ~0.3 mW with a beam spot on the samples of ~1.5 µm. We performed the Raman measurements under a microscope in backscattering configuration with linear polarized excitation and unpolarized detection. We analyzed the scattered Raman light by a spectrometer (Spectra Pro 2300i, Acton, f = 0.3 m) that was coupled to a microscope and equipped with an 1800 grooves/mm grating and a CCD camera (Pixis 256BR, Princeton Instruments). We conducted temperature-dependent measurements in a high-temperature micro-scope stage (Linkam, TS 1500) under flowing Ar at atmospheric pressure with a heating rate of 20 °C/min. We obtained a sufficient signal-to-noise ratio by using 10 s acquisition times. We calibrated the Raman system using a single-crystal Si substrate.

TEM Imaging. We performed in situ heating experiments and EDS imaging in a Hitachi HF3300 TEM/STEM equipped with a Bruker XFlash SDD detector. We used a Protochips Aduro heating system (consisting of a TEM holder, controller, power supply, and thermal E-chips) for the heating experiments. We prepared samples for analysis by dispersing the material in acetone and drop casting the solution onto the membrane heater. We performed controlled heating and cooling ramps within the microscope with the electron beam off until the set temperature was reached, except in the case of the slow quench, which we performed ex situ in a Gatan vacuum pumping system. We acquired and analyzed the STEM-EDS spectrum images in the Bruker Esprit software; for this analysis we used the Cu-L peak in lieu of the Cu-K peak to reduce the contribution of spurious Cu X-rays generated from the Aduro holder. High-energy bremßtrahlung X-ray radiation is the primary source of spurious X-rays in this TEM system and results

in a larger contribution to the Cu-K peak than to the Cu-L peak. We thus used the L-edge peak in the generation of the qualitative Cu spectrum images in Figure 7 as a precaution.

High-Resolution Synchrotron Diffraction. We characterized the ferrielectric heterostructured material with the composition $Cu_{0.42}In_{1.23}P_2S_6$ by synchrotron X-ray diffraction at the 11-ID-C beamline of the Advanced Photon Source at Argonne National Laboratory. Temperature control was enabled by use of a Linkam THMS600 heating/cooling system. We ground the samples into a fine powder and placed them in an open Cu cylinder. We sealed the holes at either end with Kapton tape and then placed the flat cylinder inside the Linkam system, which we then purged repeatedly with N_2 gas. As the chemical domain structure is sensitive to the thermal history of the sample,[23] we took diffraction patterns from low temperature to high. We varied temperatures from 93 to 623 K, allowing the system to stabilize before we collected the XRD patterns. The error in temperature over the length of the measurement was less than 0.2 K. We collected the XRD patterns in transmission mode using a Perkin−Elmer large-area detector; the wavelength of the synchrotron radiation was 0.117 418 Å. We then integrated the collected 2D patterns into conventional 1D patterns (i.e., intensity vs 2θ) for final data analysis using the Fit2d software. We performed all refinements of the resulting diffraction patterns using FullProf.[49]

Density Functional Theory. We performed DFT-based computations using the VASP package[50] together with a PBE exchange−correlation functional.[51] We assumed a Grimme (D2)-type van der Waals interaction between the layers.[52] To estimate the sizes of Cu and In hopping barriers, we created Cu vacancies in the pure $CuInP_2S_6$ ferrielectric compound, and we computed both in-plane and out-of-plane hopping barriers using the climbing-image nudged-elastic band method.[53] We obtained the formation enthalpy differences by taking the total energy differences of the structures with vacancies located at the different possible sites (see Supplementary Figure S8). The out-of-plane energy barrier for Cu hopping was about 0.85 eV, and the formation enthalpy difference was ∼11.6 meV. We performed a similar computation to calculate the In hopping barrier and formation enthalpy differences (in-plane only) in the pure $In_{4/3}P_2S_6$ phase. We performed the $In_{4/3}P_2S_6$ calculations in the unit-cell using a 2 × 1 × 1 k-mesh to integrate the Brillouin zone, and we performed the pure $CuInP_2S_6$ calculations in an enlarged 2 × 2 × 1 supercell using just a Γ point to integrate the Brillouin zone.

ASSOCIATED CONTENT

* **Supporting Information**

> Additional figures related to the thermodynamic and structural characterization; structural parameters of the HT phase (PDF)

AUTHOR INFORMATION

Corresponding Authors
*E-mail: mike.susner@gmail.com; michael.susner.ctr@us.af.mil.
*E-mail: maksymovychp@ornl.gov.
*E-mail: mcguirema@ornl.gov.
ORCID
Michael A. Susner: 0000-0002-1211-8749
Marius Chyasnavichyus: 0000-0003-3640-7200
Albina Y. Borisevich: 0000-0002-3953-8460
Notes
The authors declare no competing financial interest.

ACKNOWLEDGMENTS

REFERENCES

(1) Allen, M. J.; Tung, V. C.; Kaner, R. B. Honeycomb Carbon: A Review of Graphene. Chem. Rev. 2010, 110, 132−145.
(2) Shao, Y.; Wang, J.; Wu, H.; Liu, J.; Aksay, I. A.; Lin, Y. Graphene Based Electrochemical Sensors and Biosensors: A Review. Electro-analysis 2010, 22, 1027−1036.
(3) Di Bartolomeo, A. Graphene Schottky Diodes: An Experimental Review of the Rectifying Graphene/Semiconductor Heterojunction. Phys. Rep. 2016, 606, 1−58.
(4) Sun, D.-M.; Liu, C.; Ren, W.-C.; Cheng, H.-M. A Review of Carbon Nanotube- and Graphene-Based Flexible Thin-Film Transistors. Small 2013, 9, 1188−1205.
(5) Lv, R.; Robinson, J. A.; Schaak, R. E.; Sun, D.; Sun, Y.; Mallouk, T. E.; Terrones, M. Transition Metal Dichalcogenides and Beyond: Synthesis, Properties, and Applications of Single- and Few-Layer Nanosheets. Acc. Chem. Res. 2015, 48, 56−64.
(6) Jones, A. M.; Yu, H.; Ghimire, N. J.; Wu, S.; Aivazian, G.; Ross, J. S.; Zhao, B.; Yan, J.; Mandrus, D. G.; Xiao, D.; Yao, W.; Xu, X. Optical Generation of Excitonic Valley Coherence in Monolayer WSe_2. Nat. Nanotechnol. 2013, 8, 634−638.
(7) Wu, S.; Schaibley, J. R.; Buckley, S.; Vuckovic, J.; Feng, L.; Yan, J.; Mandrus, D. G.; Hatami, F.; Yao, W.; Majumdar, A.; Xu, X. Monolayer Semiconductor Nanocavity Lasers with Ultralow Thresholds. Nature 2015, 520, 69−72.
(8) Withers, F.; Del Pozo-Zamudio, O.; Schwarz, S.; Dufferwiel, S.; Walker, P. M.; Godde, T.; Rooney, A. P.; Gholinia, A.; Woods, C. R.; Blake, P.; Haigh, S. J.; Watanabe, K.; Taniguchi, T.; Aleiner, I. L.; Geim, A. K.; Fal'ko, V. I.; Tartakovskii, A. I.; Novoselov, K. S. WSe_2 Light-Emitting Tunneling Transistors with Enhanced Brightness at Room Temperature. Nano Lett. 2015, 15, 8223−8228.
(9) Ross, J. S.; Klement, P.; Jones, A. M.; Ghimire, N. J.; Yan, J.; Mandrus, D. G.; Taniguchi, T.; Watanabe, K.; Kitamura, K.; Yao, W.; Cobden, D. H.; Xu, X. Electrically Tunable Excitonic Light-Emitting

Diodes Based on Monolayer WSe$_2$ p-n Junctions. Nat. Nanotechnol. 2014, 9, 268−272.

(10) Lopez-Sanchez, O.; Lembke, D.; Kayci, M.; Radenovic, A.; Kis, A. Ultrasensitive Photodetectors Based on Monolayer MoS$_2$. Nat. Nanotechnol. 2013, 8, 497−501.

(11) Lee, Y. T.; Choi, W. K.; Hwang, D. K. Chemical Free Device Fabrication of Two Dimensional van Der Waals Materials Based Transistors by Using One-off Stamping. Appl. Phys. Lett. 2016, 108, 253105.

(12) Pizzocchero, F.; Gammelgaard, L.; Jessen, B. S.; Caridad, J. M.; Wang, L.; Hone, J.; Bøggild, P.; Booth, T. J. The Hot Pick-up Technique for Batch Assembly of van Der Waals Heterostructures. Nat. Commun. 2016, 7, 11894.

(13) Wu, Q.; Wongwiriyapan, W.; Park, J.-H.; Park, S.; Jung, S. J.; Jeong, T.; Lee, S.; Lee, Y. H.; Song, Y. J. In Situ Chemical Vapor Deposition of Graphene and Hexagonal Boron Nitride Hetero-structures. Curr. Appl. Phys. 2016, 16, 1175−1191.

(14) Susner, M. A.; Chyasnavichyus, M.; McGuire, M. A.; Ganesh, P.; Maksymovych, P. Metal Thio- and Selenophosphates as Multi-Functional van Der Waals Layered Materials. Advanced Materials 2017, in press.

(15) Joy, P. A.; Vasudevan, S. Magnetism in the Layered Transition-Metal Thiophosphates MPS$_3$ (M = Manganese, Iron, and Nickel). Phys. Rev. B: Condens. Matter Mater. Phys. 1992, 46, 5425−5433.

(16) Clement, R.; Leaustic, A. Intercalation-Induced Magnetization in MPS$_3$ Layered Compounds. In Magnetism and Molecular Materials II; Wiley-VCH Verlag GmbH, 2001; pp 397−423.

(17) Colombet, P.; Leblanc, A.; Danot, M.; Rouxel, J. Structural Aspects and Magnetic Properties of the Lamellar Compound Copper Chromium Phosphorotrithioite (Cu$_{0.50}$Cr$_{0.50}$PS$_3$). J. Solid State Chem. 1982, 41, 174−184.

(18) Lee, S.; Colombet, P.; Ouvrard, G.; Brec, R. A New Chain Compound of Vanadium(III): Silver Vanadium Thiophosphate (Ag$_{1/2}$V$_{1/2}$PS$_3$) Structure, Metal Ordering, and Magnetic Properties. Mater. Res. Bull. 1986, 21, 917−928.

(19) Zhukov, V.; Alvarez, S.; Novikov, D. Electronic Band Structure of the Magnetic Layered Semiconductors MPS$_3$ (M = Mn, Fe and Ni). J. Phys. Chem. Solids 1996, 57, 647−652.

(20) Manova, E.; Leustic, A.; Mitov, I.; Gonbeau, D.; Clement, R. The NiPS$_3$-Cobaltocene Intercalation Compound: A New Ferromag-net. Mol. Cryst. Liq. Cryst. Sci. Technol., Sect. A 1998, 311, 563−568.

(21) Maisonneuve, V.; Payen, C.; Cajipe, V. B. On CuCrP$_2$S$_6$: Copper Disorder, Stacking Distortions, and Magnetic Ordering. J. Solid State Chem. 1995, 116, 208−210.

(22) Wildes, A. R.; Simonet, V.; Ressouche, E.; McIntyre, G. J.; Avdeev, M.; Suard, E.; Kimber, S. A. J.; Lancon, D.; Pepe, G.; Moubaraki, B.; Hicks, T. J. Magnetic Structure of the Quasi-Two-Dimensional Antiferromagnet NiPS$_3$Phys. Rev. B: Condens. Matter Mater. Phys.2015, 92, 10.1103/PhysRevB.92.224408.

(23) Susner, M. A.; Belianinov, A.; Borisevich, A. Y.; He, Q.; Chyasnavichyus, M.; Ganesh, P.; Demir, H.; Sholl, D.; Abernathy, D. L.; McGuire, M. A.; Maksymovych, P. High T$_c$ Layered Ferrielectric Crystals by Coherent Spinodal Decomposition. ACS Nano 2015, 9, 12365−12373.

(24) Ievlev, A. V.; Susner, M. A.; McGuire, M. A.; Maksymovych, P.; Kalinin, S. V. Quantitative Analysis of the Local Phase Transitions Induced by Laser Heating. ACS Nano 2015, 9, 12442−12450.

(25) Belianinov, A.; Iberi, V. O.; Tselev, A.; Susner, M. A.; McGuire, M. A.; Joy, D.; Jesse, S.; Rondinone, A. J.; Kalinin, S. V.; Ovchinnikova, O. S. Polarization Control via He-Ion Beam Induced Nanofabrication in Layered Ferroelectric Semiconductors. ACS Appl. Mater. Interfaces 2016, 8, 7349−7355.

(26) Belianinov, A.; He, Q.; Maksymovych, P.; Borisevich, A.; Kalinin, S. V.; Dziaugys, A.; Banys, J.; Eliseev, E.; Morozovska, A.; Vysochanskii, Y. CuInP$_2$S$_6$ Room Temperature Layered Ferroelectric. Nano Lett. 2015, 15, 3808−3814.

(27) Dziaugys, A.; Banys, J.; Samulionis, V.; Macutkevic, J.; Vysochanskii, Y.; Shvartsman, V.; Kleemann, W. Phase Transitions in Layered Semiconductor - Ferroelectrics. In Ferroelectrics: Character-ization and Modeling; InTech, 2011; pp 153−180.

(28) Dziaugys, A.; Banys, J.; Macutkevic, J.; Vysochanskii, J. Conductivity Spectroscopy of New AgInP$_2$S$_6$ Crystals. Integr. Ferroelectr. 2008, 103, 52−59.

(29) Maisonneuve, V.; Cajipe, V. B.; Simon, A.; Von Der Muhll, R.; Ravez, J. Ferrielectric Ordering in Lamellar CuInP$_2$S$_6$. Phys. Rev. B: Condens. Matter Mater. Phys. 1997, 56, 10860−10868.

(30) Kamata, A.; Noguchi, K.; Suzuki, K.; Tezuka, H.; Kashiwakura, T.; Ohno, Y.; Nakai, S.-I. Resonant 2p → 3d Photoemission Measurement of MPS$_3$ (M = Mn, Fe, Ni). J. Phys. Soc. Jpn. 1997, 66, 401−407.

(31) Chyasnavichyus, M.; Susner, M. A.; Ievlev, A. V.; Eliseev, E. A.; Kalinin, S. V.; Balke, N.; Morozovska, A. N.; McGuire, M. A.; Maksymovych, P. Size-Effect in Layered Ferrielectric CuInP$_2$S$_6$. Appl. Phys. Lett. 2016, 109, 172901.

(32) Delaney, M. J.; Ushioda, S. Raman Spectra of Silver-Halide Melts and Sublattice Melting in the Superionic Conductor α- AgI. Phys. Rev. B 1977, 16, 1410.

(33) Boyce, J. B.; Hayes, T. M.; Mikkelsen, J. C., Jr Extended-x-Ray-Absorption-Fine-Structure Investigation of Mobile-Ion Density in Superionic AgI, CuI, CuBr, and CuCl. Phys. Rev. B: Condens. Matter Mater. Phys. 1981, 23, 2876.

(34) Park, K.-Y.; Park, I.; Kim, H.; Lim, H.; Hong, J.; Kim, J.; Kang, K. Anti-Site Reordering in LiFePO$_4$: Defect Annihilation on Charge Carrier Injection. Chem. Mater. 2014, 26, 5345−5351.

(35) Dathar, G. K. P.; Balachandran, J.; Kent, P. R. C.; Rondinone, A. J.; Ganesh, P. Li-Ion Site Disorder Driven Superionic Conductivity in Solid Electrolytes: A First-Principles Investigation of Beta-Li$_3$PS$_4$. J. Mater. Chem. A 2017, 5, 1153−1159.

(36) Lubimtsev, A. A.; Kent, P. R. C.; Sumpter, B. G.; Ganesh, P. Understanding the Origin of High-Rate Intercalation Pseudocapaci-tance in Nb$_2$O$_5$ Crystals. J. Mater. Chem. A 2013, 1, 14951.

(37) Lee, S.; Sun, X.-G.; Lubimtsev, A. A.; Gao, X.; Ganesh, P.; Ward, T. Z.; Eres, G.; Chisholm, M. F.; Dai, S.; Lee, H. N. Persistent Electrochemical Performance in Epitaxial VO$_2$. Nano Lett. 2017, 17, 2229−2233.

(38) Gebesh, V. Y.; Potorii, M. V.; Voroshilov, Y. V. Phase Equilibrium in the In-P-S System. Ukr. Khim. Zhurn. 1991, 57, 803− 806.

(39) Shusta, V. S.; Prits, I. P.; Guranich, P. P.; Gerzanich, E. I.; Slivka, A. G. Dielectric Properties of CuInP$_2$S$_6$ Crystals under High Pressure. Condens. Matter Phys. 2007, 49, 91−94.

(40) Hahn, H.; Klingen, W. Sulfide and Selenide Phosphides of Iron, Cobalt, and Nickel. Naturwissenschaften 1965, 52, 494.

(41) Friedel, C. Thiohypophosphates. Compt. Rend. 1894, 119, 260−264.

(42) Fujioka, Y.; Frantti, J.; Puretzky, A.; King, G. Raman Study of the Structural Distortion in the Ni$_{1−x}$Co$_x$TiO$_3$ Solid Solution. Inorg. Chem. 2016, 55, 9436−9444.

(43) Vysochanskii, Y. M.; Stephanovich, V. A.; Molnar, A. A.; Cajipe, V. B.; Bourdon, X. Raman Spectroscopy Study of the Ferrielectric-Paraelectric Transition in Layered CuInP$_2$S$_6$. Phys. Rev. B: Condens. Matter Mater. Phys. 1998, 58, 9119−9124.

(44) Boulfelfel, S. E.; Zahn, D.; Hochrein, O.; Grin, Y.; Leoni, S. Low-Dimensional Sublattice Melting by Pressure: Superionic Con-duction in the Phase Interfaces of the Fluorite-to-Cotunnite Transition of CaF$_2$. Phys. Rev. B: Condens. Matter Mater. Phys. 2006, 74, 094106.

(45) Boyce, J. B.; Mikkelsen, J. C.; O'Keeffe, M. Ion Dynamics and Sublattice Melting in the Superionic Conductor PbF$_2$. Solid State Commun. 1977, 21, 955−958.

(46) Hainovsky, N.; Maier, J. Simple Phenomenological Approach to Premelting and Sublattice Melting in Frenkel Disordered Ionic Crystals. Phys. Rev. B: Condens. Matter Mater. Phys. 1995, 51, 15789.

(47) Perez, M. Gibbs-Thomson Effects in Phase Transformations. Scr. Mater. 2005, 52, 709−712.

(48) Sales, B. C. Structural Relaxation Dynamics of Phosphate Glasses: The Effects of Network Topology on the Glass Transition. J. Non-Cryst. Solids 1990, 119, 136−150.

(49) Frontera, C.; Rodriguez-Carvajal, J. FULLPROF as a New Tool for Flipping Ratio Analysis: Further Improvements. Phys. B 2004, 350, e731−e733.

(50) Kresse, G.; Furthmueller, J. Efficient Iterative Schemes for Ab Initio Total-Energy Calculations Using a Plane-Wave Basis Set. Phys. Rev. B: Condens. Matter Mater. Phys. 1996, 54, 11169−11186.

(51) Perdew, J. P.; Burke, K.; Ernzerhof, M. Generalized Gradient Approximation Made Simple. Phys. Rev. Lett. 1996, 77, 3865−3868.

(52) Grimme, S. Semiempirical GGA-Type Density Functional Constructed with a Long-Range Dispersion Correction. J. Comput. Chem. 2006, 27, 1787−1799.

(53) Henkelman, G.; Uberuaga, B. P.; Jonsson, H. A Climbing Image Nudged Elastic Band Method for Finding Saddle Points and Minimum Energy Paths. J. Chem. Phys. 2000, 113, 9901−9904.